Assessment of hybrid rotation-translation scan schemes for *in vivo* animal SPECT imaging

2013 Phys. Med. Biol. 58 965

(http://iopscience.iop.org/0031-9155/58/4/965)

Phys. Med. Biol. **58** (2013) 965–983 doi:10.1088/0031-9155/58/4/965

Assessment of hybrid rotation-translation scan schemes for *in vivo* animal SPECT imaging

Yan Xia[1,2], **Rutao Yao**[3], **Xiao Deng**[3], **Yaqiang Liu**[1,2], **Shi Wang**[1,2] **and Tianyu Ma**[1,2]

[1] Department of Engineering Physics, Tsinghua University, Beijing 100084, People's Republic of China
[2] Key Laboratory of Particle & Radiation Imaging, Ministry of Education, People's Republic of China
[3] Department of Nuclear Medicine, State University of New York at Buffalo, Buffalo, New York 14214, USA

E-mail: maty@tsinghua.edu.cn

Received 19 March 2012, in final form 13 December 2012
Published 23 January 2013
Online at stacks.iop.org/PMB/58/965

Abstract

To perform *in vivo* animal single photon emission computed tomography imaging on a stationary detector gantry, we introduced a hybrid rotation-translation (HRT) tomographic scan, a combination of translational and limited angle rotational movements of the image object, to minimize gravity-induced animal motion. To quantitatively assess the performance of ten HRT scan schemes and the conventional rotation-only scan scheme, two simulated phantoms were first scanned with each scheme to derive the corresponding image resolution (*IR*) in the image field of view. The *IR* results of all the scan schemes were visually assessed and compared with corresponding outputs of four scan scheme evaluation indices, i.e. sampling completeness (*SC*), sensitivity (*S*), conventional system resolution (*SR*), and a newly devised directional spatial resolution (*DR*) that measures the resolution in any specified orientation. A representative HRT scheme was tested with an experimental phantom study. Eight of the ten HRT scan schemes evaluated achieved a superior performance compared to two other HRT schemes and the rotation-only scheme in terms of phantom image resolution. The same eight HRT scan schemes also achieved equivalent or better performance in terms of the four quantitative indices than the conventional rotation-only scheme. As compared to the conventional index *SR*, the new index *DR* appears to be a more relevant indicator of system resolution performance. The experimental phantom image obtained from the selected HRT scheme was satisfactory. We conclude that it is feasible to perform *in vivo* animal imaging with a HRT scan scheme and *SC* and *DR* are useful predictors for quantitatively assessing the performance of a scan scheme.

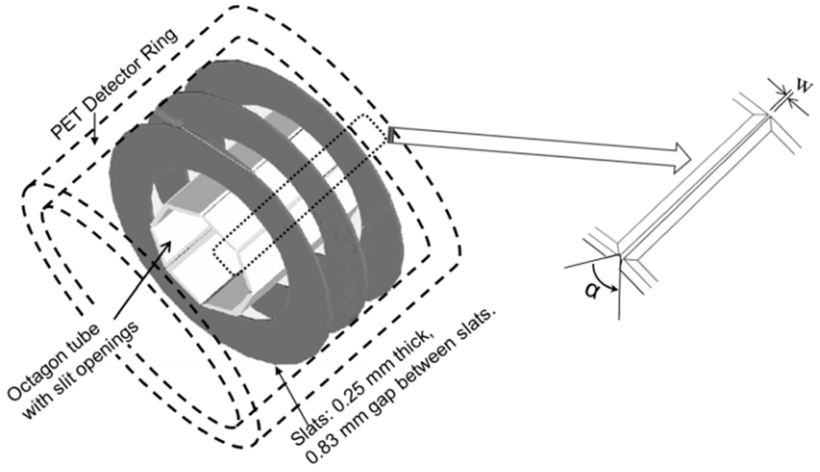

Figure 1. The setup of the add-on SPECT prototype. The slit-slat collimator insert is inside the animal PET scanner's detector ring for SPECT imaging. Only three slats are shown for clarity.

1. Introduction

Small animal single photon emission computed tomography (SPECT) is an essential tool for preclinical biomedical research (Meikle *et al* 2005). To expand the availability of SPECT, we developed an add-on SPECT technology (Shao *et al* 2007, Yao *et al* 2009, Ma *et al* 2009) that enables an animal positron emission tomography (PET) scanner to also perform SPECT imaging. The add-on SPECT uses the same PET detector gantry and electronics for detecting gamma events, and the only new hardware component used is a collimator insert placed inside the PET detector ring. This technology provides the benefits of lower overall cost for a PET/SPECT dual function systems and potential PET/SPECT dual tracer applications.

Figure 1 illustrates the setup of the add-on SPECT prototype system that we developed. The collimator insert is a slit-slat collimator which consists of a lead octagon tube and multiple tungsten annular slats stacks in the tube's axial direction. The slit openings are along the vertical edges of the octagon tube. We selected a slit-slat collimator because it offers several attractive features (Rogers *et al* 1982, Metzler and Jaszczak 2006, Mahmood *et al* 2009, Chang *et al* 2009, Metzler *et al* 2006, Li *et al* 2009). First, the fan-beam projections through the slits offer a magnification factor which could be useful for improving the imaging resolution in the transverse plane. Second, the parallel collimation through the slats defines an axial field-of-view (FOV) that is equal to the extent of the slats. So with a stack of slats, a large axial FOV is readily achieved for whole body animal imaging. Third, the slats effectively segment the 3D imaging volume into multiple 2D imaging planes. The 2D tomographic image formation theory is well established and the scan scheme design is much simplified as compared to that for 3D imaging. For ease in mechanical implementation, the collimator insert was assembled in a single module and placed at a fixed position inside the PET detector ring. So both the collimator assembly and detector ring are stationary, only the imaging object is mobile.

To perform tomographic data acquisition on this system, the conventional scheme is to rotate the imaging object around the axial axis to acquire projection views over a 180° or 360° angular range. However, this option is problematic for imaging animals *in vivo*. Due to the effect of gravity, the body shape and organ positions of the animal would move during the

rotational scan process, as a live animal's body cannot be rigidly constrained. The body and organ movements would compromise the quality of imaging data acquired. For good quality *in vivo* studies, a scan scheme with minimal rotation must be developed.

A variety of scan schemes have been reported in the literature or implemented in commercial SPECT systems. While the general principle for all scan schemes is to satisfy the sufficiency condition for complete sampling (Orlov 1976), the choice of a particular scan scheme is system specific. For example, most of pinhole-based systems use a helical scanning orbit (Metzler *et al* 2003a, DiFilippo 2008) for artifact free volume imaging and more uniform imaging performance along the axial direction. But for U-SPECT-I system, only translational movement of the imaging object is used. This is because U-SPECT-I has a sufficient number of pinholes arranged at appropriate view angles (Beekman *et al* 2004); even without any rotation of object or detector involved, the projection sampling is still adequate for a small targeted volume. Translational movement was used on U-SPECT-I only to expand the FOV for whole-body animal imaging (Vastenhouw and Beekman 2007). Another example is the Linoview system (Walrand *et al* 2005). Due to its unique collimator design, the collimator and detector assembly were moved linearly instead of rotationally to achieve tomographic imaging.

The goal of this work was to assess the performance of hybrid rotation-translation (HRT) scan schemes for *in vivo* animal imaging, i.e. only small-angle rotation is allowed, on the add-on SPECT system. Due to the slit-slat collimator's 2D fan-beam imaging geometry, we focused on studying the transverse in-plane movement schemes and imaging performance in this work; the patterns of the simulated and experimental phantoms were designed or selected accordingly. Axial movements and performance considerations were not included.

2. Materials and methods

2.1. Detector and collimator insert

The animal PET scanner used in this study was a microPET Focus-120 system (Siemens Preclinical Solutions, Knoxville, TN). It consisted of four detector rings with a 14.7 cm diameter and 7.6 cm axial extent (Laforest *et al* 2007). The bore opening of the scanner was 13.5 cm, which was the maximum diameter that the slit-slat collimator assembly could fit in. Each detector ring had 24 detector blocks. Each block consisted of a 12×12 array of lutetium oxyorthosilicate (LSO) crystals and each crystal had a pitch of $1.6 \times 1.6 \times 10\ \text{mm}^3$.

The slit-slat collimator used is shown in figure 1. The slit tube was made of lead and the slats were made of tungsten. The center-to-center distance between the octagon tube's opposite lead-plates was 64.5 mm. The thickness of the plates was 2.5 mm. The radius of the slit aperture was 33 mm. The slit-apertures' opening angle α was 90° and the slit-opening width w was 0.6 mm. The slit-aperture positions and opening angle were selected so that the PET ring detectors were fully utilized without projection overlapping. There were a total of 70 slats covering an axial field-of-view of 75 mm (only three slats are shown in figure 1 for clarity). The inner and outer diameters of the slats were 84 and 132 mm, respectively. The thickness of the slats was 0.25 mm. Two concentric, narrow radial width ($\sim$1.5 mm), plastic rings were placed between neighboring slats as spacers. Figure 2 shows a slat with two spacer rings attached to it. The spacers' thickness was 0.83 mm. The centers of the slats were stacked in parallel to the axial axis of the slit tube and the animal PET detector ring.

2.2. HRT scan scheme

A HRT scheme is a sequence of combined translational and rotational movements of the imaging object. The rational of the HRT scan is to use object translational movement to

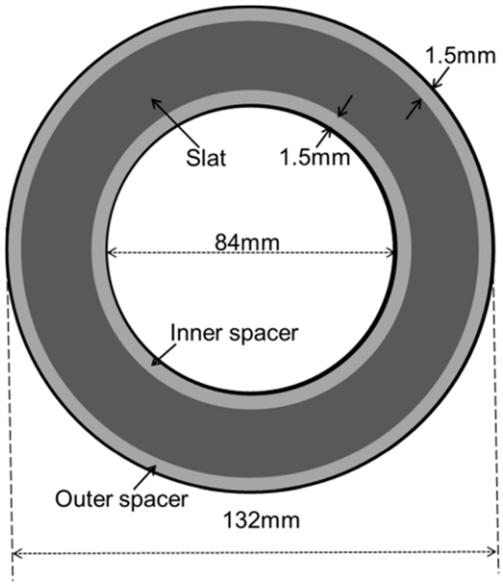

Figure 2. Illustration of a slat with inner and outer ring spacers attached.

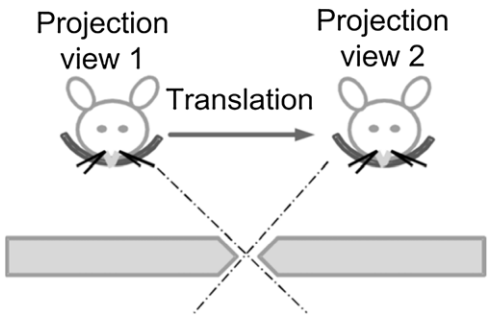

Figure 3. Translational movement of object provides projection views of the object from different angles.

obtain projections at different views; therefore, the object rotation can be reduced, or ideally, eliminated. This is illustrated in figure 3. The image object is moved from left to right horizontally—a translational movement. Two projection views, 1 and 2, can be acquired as the object is seen from different angles through the slit aperture.

We designed ten HRT schemes by permuting two translational paths and five rotational settings. The two translational paths are denoted as R and G to represent the *round* and *grid* path patterns, respectively. The paths are shown as dashed lines in figure 4. The rotational movements of the object, usually by a set of discrete angles, take place at each stop of a translational path. To facilitate the comparison of different scan schemes, each HRT scan scheme is denoted by a code. The code is a combination of the translation path indicator, i.e. R or G, and the number of the rotation steps. For example, R2 stands for a scan scheme that follows the R translation path and has two rotation steps at each translational stop. The specific settings of all ten HRT scan schemes are described in table 1.

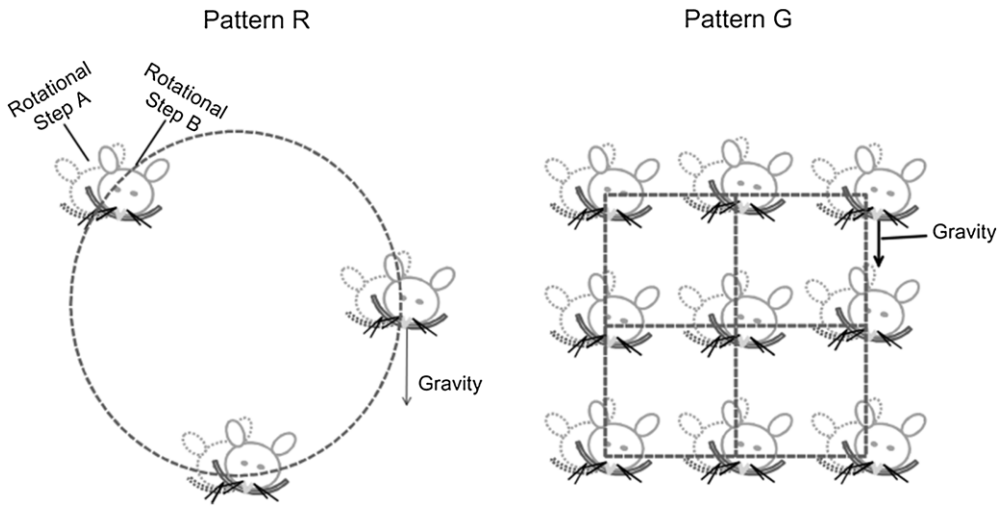

Figure 4. Illustration of the concept of the HRT scan. The translational movement paths R and G are shown in the left and right diagrams, respectively. The animal stays on bed in a prone position. At each translational movement stop, the bed is rotated to a few angular positions to provide additional projection views of the animal.

Table 1. Settings of the ten HRT scan schemes studied. The radius of the scanning path of R schemes is 6.5 mm.

Scheme code	Number of rotational steps (rotational angles)	Number of translational steps (angular interval)	Scheme code	Number of rotational steps (rotational angles)	Number of translational steps (grid interval)
R1	1 (0°)	120 (3°)	G1	1 (0°)	11 × 11 (1.1 mm)
R2	2 (−10°,10°)	60 (6°)	G2	2 (−10°,10°)	8 × 8 (1.57 mm)
R3	3 (−10°,0°,10°)	40 (9°)	G3	3 (−10°,0°,10°)	6 × 6 (2.20 mm)
R4	4 (−10°,−3°,3°,10°)	30 (12°)	G4	4 (−10°,−3°,3°,10°)	5 × 5 (2.75 mm)
R5	5 (−10°,−5°,0°,5°,10°)	24 (15°)	G5	5 (−10°,−5°,0°,5°,10°)	5 × 5 (2.75 mm)

The conventional 360° rotation-only scan scheme, denoted by code O, was used as the reference scheme. With the O scan scheme, a set of projection data is acquired after each rotational stop. With a HRT scheme, either it is R or G, the object is first moved through its translational path. At each translational stop, the object is rotated through its rotational stops. A set of projection data is acquired at each rotational stop. R1 and G1 are two special HRT schemes that consist of only translational movements.

2.3. Scan scheme performance evaluation indices

Four indices were defined to quantitatively assess the performance of the scan schemes: sampling completeness (*SC*), sensitivity (*S*), conventional system resolution (*SR*) and directional resolution (*DR*).

The concept of index *SC* is similar to that of *SC*(%) defined for pinhole SPECT (Metzler *et al* 2003b). In this study *SC* was defined as the percentage of the projection views that a scan scheme acquires over the ideal complete projection views for 2D tomographic imaging. It is

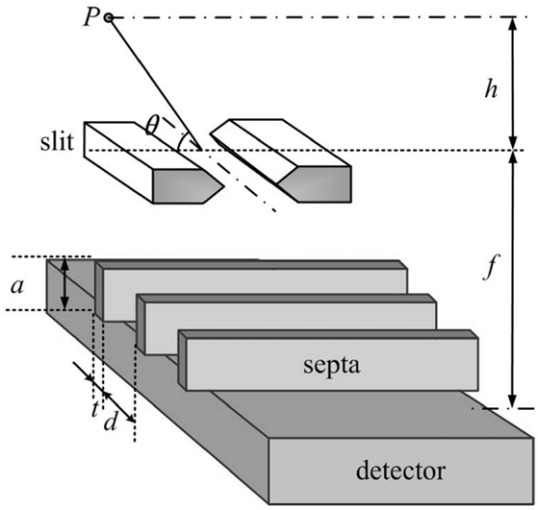

Figure 5. Illustration of a slit-slat collimator's geometrical parameters used in this work.

an explicit translation of the requirement for 2D Radon transform theorem (Radon 1986). *SC* was calculated by the following formula:

$$SC = (m/n) \times 100\%, \tag{1}$$

where m is the total number of projection views acquired with a scan scheme, and n is the number of projection views required for adequately sampling 360°. In this work, we chose $n = 120$, for most orbits contain only 120 shoot step which provides 120 different view angles at most. For a scan scheme, the 360° view angle range is uniformly divided into n bins with a bin size of 360°/n or 3°, and m is the number of the bins that have at least one projection view collected in it.

Sensitivity S is derived directly from the standard system detection efficiency. The S at point P of image object is calculated as the sum of contributions of sensitivity from each slit and at each scan step (Accorsi *et al* 2008), which is

$$S = \sum_{j}^{J} \sum_{i=1}^{I} S_{i,j}, \tag{2}$$

$$S_{i,j} = \frac{w_{\text{eff , sens}} d^2}{4\pi (d+t) a h_{i,j}} \sin^3 \theta_{i,j}, \tag{3}$$

where $S_{i,j}$ stands for the sensitivity acquired through ith slit at jth scan step, I is the total number of slits, i.e. eight, in this study, and J is the total number of movement steps for a scan scheme. As is illustrated in figure 5, h is the distance from P to the slit plane, θ is the projection incidence angle, w and α are slits' opening width and angle, respectively, d is the gap between the slats, a is the slat's radial height, t is the slat thickness. $w_{\text{eff,sens}}$ is the sensitivity equivalent effective slit width (Novak *et al* 2008),

$$w_{\text{eff,sens}} = w + \frac{1}{\mu} \cdot \left(1 - \cot^2 \frac{\alpha}{2} \cot^2 \theta\right) \cdot \sin\theta \cdot \tan \frac{\alpha}{2}. \tag{4}$$

System resolution (*SR*) is a widely used index in collimator design (Beekman and Vastenhouw 2004, Novak *et al* 2008). The *SR* at *P* calculated from the ith slit at jth scan step is

$$SR_{i,j} = \sqrt{R_{\text{det}}^2 \cdot \left(\frac{h_{i,j}}{f}\right)^2 + w_{\text{eff,reso}}^2 \cdot \left(1 + \frac{h_{i,j}}{f}\right)^2} \tag{5}$$

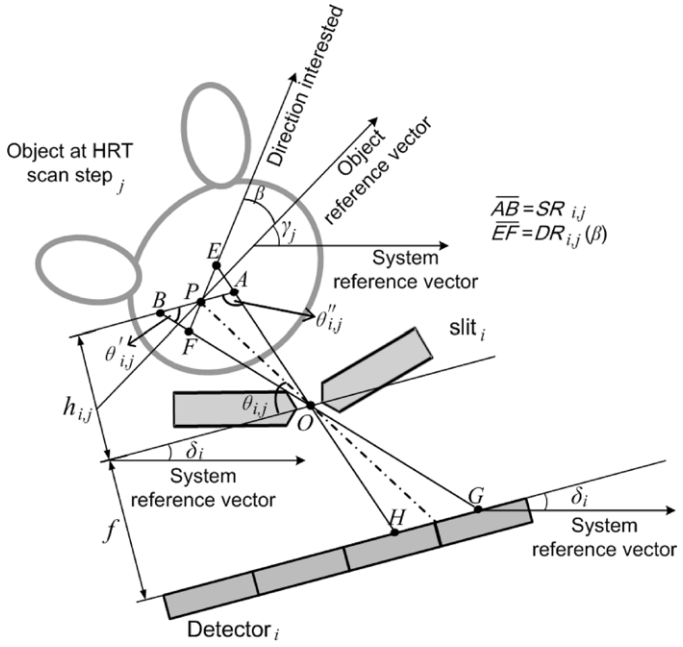

Figure 6. Illustration of the definition of directional resolution. Line *EF* passes the interested image pixel *P*. Its direction angle is β relative to the object reference vector. In a simplified projection model, image distributions from both lines *EF* and *AB* may form the same projection line *GH* on the detector. The length of $\overline{AB}$is the convertional $SR_{i,j}$, the length of $\overline{EF}$is defined as $DR_{i,j}(\beta)$.

where $w_{\text{eff,reso}} = w - \frac{\ln(0.5)}{\mu} \cdot \sin\theta \cdot \cot\frac{\alpha}{2} \cdot \left(\tan^2\frac{\alpha}{2} - \cot^2\theta\right)$ (Novak *et al* 2008), R_{det} is detector's intrinsic resolution, f is the radial distance from the slit aperture center to the detector ring, and $w_{\text{eff,reso}}$ is the resolution equivalent effective slit width. As the pitch of the pixelated detector scintillators is 1.59 mm, $R_{\text{det}} = 1.59$ mm.

For a scan that acquires and uses many projections for tomographic imaging, the conventional weighted average of $SR_{i,j}$ from all slit apertures and for all movement steps, is used to measure the average system resolution (Beekman and Vastenhouw 2004), i.e.

$$SR_{\text{conv}} = \frac{\sum_{j=1}^{J}\sum_{i=1}^{I} S_{i,j} \times SR_{i,j}}{\sum_{j=1}^{J}\sum_{i=1}^{I} S_{i,j}}. \tag{6}$$

The conventional system resolution *SR* is insufficient for describing the complete relationship between an emission source and the resulting projection. As illustrated in figure 6, *SR* is represented by the line segment *AB* in the emission space; it is the back-projection of line segment *GH*, the corresponding projection resolution on the detector side. The conventional *SR* derivation is based on the assumption that *AB* and *GH* are parallel. However, the emission distribution passing through *P* is not limited to be along *AB* only. Other emission distributions such as the one represented by line segment *EF* may form the same projection *GH*. To evaluate the image spatial resolution in different directions, such as *EF*, we introduce a new resolution measure, the directional resolution $DR_{i,j}(\beta)$, to account for the effect of the angle β, the emission source's distribution orientation.

To calculate the directional resolution *EF* in figure 6, we first define a reference vector to represent the image object's orientation. *EF* has an angle β relative to the object reference vector. The reference vector represents a fixed reference frame that is attached to the object.

For example, it may start at the center of a mouse's left eye, and point toward the center of the right eye. When the object or animal is rotated, the reference vector's orientation changes relative to the imaging system's coordinate frame. As shown in figure 6, the object reference vector's orientation angle at jth scan step is γ_j relative to the imaging system reference vector.

For the SPECT system described in this work, all the slits are stationary relative to the detector gantry. Each slit opening is parallel to the detector surface behind it. The orientation angle of the ith slit opening is denoted by δ_i, as shown in figure 6.

By applying the sine theorem in $\Delta PEA$and ΔPFB, the directional resolution $DR_{i,j}\ (\beta)$for a projection passing through ith slit and at the jth object movement step is

$$\begin{aligned} DR_{i,j}(\beta) &= \overline{EF} \\ &= \overline{EP} + \overline{PF} \\ &= \left[\left|\frac{\overline{AP}\cdot\sin\theta''_{i,j}}{\sin\left(\theta''_{i,j}-\beta-\gamma_j+\delta_i\right)}\right| + \left|\frac{\overline{PB}\cdot\sin\theta'_{i,j}}{\sin\left(\theta'_{i,j}+\beta+\gamma_j-\delta_i\right)}\right|\right] \\ &= \frac{SR_{i,j}}{2}\times\left[\left|\frac{\sin\theta''_{i,j}}{\sin\left(\theta''_{i,j}-\beta-\gamma_j+\delta_i\right)}\right| + \left|\frac{\sin\theta'_{i,j}}{\sin\left(\theta'_{i,j}+\beta+\gamma_j-\delta_i\right)}\right|\right]. \end{aligned} \tag{7}$$

By applying the cosine theorem inΔOPAandΔOPB, one has

$$\theta'_{i,j} = \arccos\left(\frac{\overline{OB}^2 + \frac{SR_{i,j}^2}{4} - \overline{OP}^2}{SR_{i,j}\times\overline{OB}}\right), \tag{8}$$

$$\theta''_{i,j} = \arccos\left(\frac{\overline{OA}^2 + \frac{SR_{i,j}^2}{4} - \overline{OP}^2}{SR_{i,j}\times\overline{OA}}\right), \tag{9}$$

and

$$\overline{OP} = \frac{h_{i,j}}{\sin\theta_{i,j}}, \tag{10}$$

$$\overline{OB} = \sqrt{\overline{OP}^2 + \frac{SR_{i,j}^2}{4} + \overline{OP}\cdot SR_{i,j}\cdot\cos\theta_{i,j}}, \tag{11}$$

$$\overline{OA} = \sqrt{\overline{OP}^2 + \frac{SR_{i,j}^2}{4} - \overline{OP}\cdot SR_{i,j}\cdot\cos\theta_{i,j}}. \tag{12}$$

Due to the possibility of infinite values of $DR_{i,j}(\beta)$, i.e. when the direction of line FE overlaps with that of line OP, it is not feasible to use (6) to calculate the weighted average of all $DR_{i,j}(\beta)$. So we propose to calculate the overall DR by the following:

$$DR\,(\beta) = \left[\frac{\sum_{j=1}^{J}\sum_{i=1}^{I} S_{i,j}^{q} DR_{i,j}\,(\beta)^p}{\sum_{j=1}^{J}\sum_{i=1}^{I} S_{i,j}^{q}}\right]^{\frac{1}{p}}, \tag{13}$$

where p and q are the numerical values that weigh in the effect of the resolution factor $DR_{i,j}(\beta)$ and the sensitivity factor $S_{i,j}$ respectively; they were determined to be -1 and 3, respectively, through a numerical searching procedure described in the appendix.

Without losing generality, $\beta = 0$, which is the direction parallel to the object reference vector, was evaluated as a test case in the remainder of this paper.

2.4. Monte Carlo simulation studies

Two phantoms were studied through Monte Carlo simulation with the GATE package (Jan *et al* 2004). The first phantom used the same specification of the ultra-micro hot-rod phantom (Data Spectrum Inc., Hillsborough, NC). The diameters of the rods in the six sections were 2.4, 2.0, 1.7, 1.35, 1.0 and 0.75 mm, respectively. The center-to-center distance in each section was twice that of the rod diameter. The height of the hot rods was 30 mm. The total activity of ^{99m}Tc source in the hot rods was 4.6 mCi. The phantom was scanned by each of the scan schemes listed in table 1, with the acquisition time of 6000 s for each scan. The second phantom consisted of 80 hot rods which were arranged in a grid pattern. Each rod was 0.25 mm in diameter and 30 mm in height. The distance between adjacent rods was 2.5 mm. A total of 1 mCi ^{99m} Tc solution was uniformly distributed in the rods. A set of SPECT data was acquired with each of the scan schemes studied. The total acquisition time for each scheme was 1 min.

For both phantom studies, the energy window used was 120–160 keV. An ML-EM algorithm was used to reconstruct the simulated data. The system matrix used was derived from a Monte Carlo simulation (Yao *et al* 2009). The voxel size of the reconstructed image was $0.25 \times 0.25 \times 1$ mm^3.

The reconstructed images of the grid-patterned hot-rod phantom were filtered with a 2D Gaussian function (FWHM = 0.075 mm). Each rod in the images was fitted with a 2D Gaussian function to extract the rod's horizontal image resolution (*IR*) in terms of FWHM. The congregation of the rod resolutions form an image, represented by $IR(\beta)|_{\beta=0}$, for comparison with the corresponding *SR* and $DR(\beta)|_{\beta=0}$ images. Only rods in the central FOV were used for the extraction of resolution to avoid issues in the edge area due to reconstruction.

2.5. Analytical evaluation

A 25 mm diameter disc was scanned hypothetically with the scan schemes described in table 1. For each scheme, the values of *SC*, *S*, *SR* and $DR(\beta)|_{\beta=0}$ at each pixel center of the disc were calculated with equations (1), (2), (6) and (13), respectively. The pixel size of the disc was set to 2.5 mm $\times$ 2.5 mm to match that of the $IR(\beta)|_{\beta=0}$ image of the grid-patterned hot-rod phantom.

To quantify the closeness between the resolution indices, such as between *IR* and *SR*, we introduced the normalized mean square error (NMSE):

$$\text{NMSE} = \frac{\sum_{x=0}^{N-1}\sum_{y=0}^{N-1}(f_A(x,y) - f_B(x,y))^2}{\sum_{x=0}^{N-1}\sum_{y=0}^{N-1} f_B(x,y)^2}, \tag{14}$$

where $f_A(x,y)$ is the image of one resolution index, e.g., *SR*, normalized to its average value, x and y are image pixel indices, $f_B(x,y)$ is the image of another resolution index, e.g., *IR*, normalized to its average value, and N is the size of images.

The NMSE in (14) is for one scan scheme. We define a joint NMSE that accounts for all the 11 schemes:

$$\text{joint-NMSE} = \frac{\sum_{\text{orbit}=O,R1,\ldots,R5,G1,\ldots,G5}\sum_{x=0}^{N-1}\sum_{y=0}^{N-1}(f_A(x,y) - f_B(x,y))^2}{\sum_{\text{orbit}=O,R1,\ldots,R5,G1,\ldots,G5}\sum_{x=0}^{N-1}\sum_{y=0}^{N-1} f_B(x,y)^2}. \tag{15}$$

2.6. Experimental hot-rod phantom

An ultra-micro hot-rod phantom (Data Spectrum Inc., Hillsborough, NC) was scanned with the conventional O scheme and the HRT G5 scheme. The diameters and the center-to-center

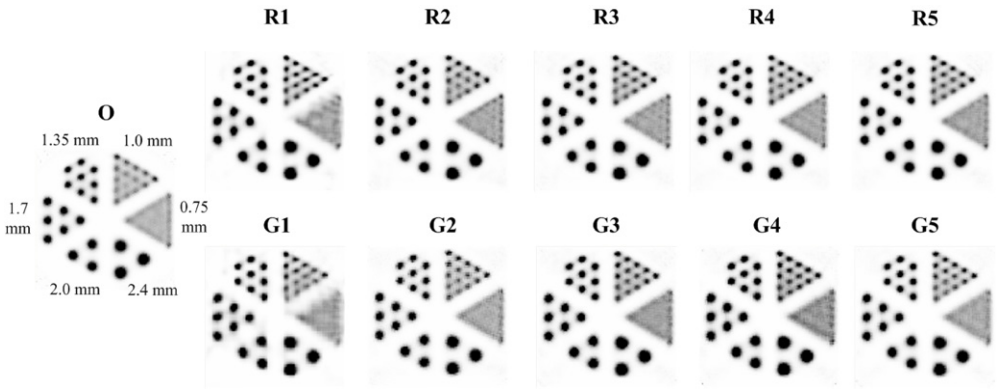

Figure 7. The ultra-micro hot-rod phantom images with Monte Carlo simulated data acquired from all the scan schemes studied. The same color palette scale setting was used for all the images, which was empirically determined to show the optimal rod identification in the smallest rod section.

distances of the hot rods were the same as described in section 2.4. The phantom was filled with 5.85 mCi ^{99m}Tc. The total scan time was 180 min and 187.5 min with the O and G5 scan scheme, respectively. The G5 scheme was picked as the representative experimental HRT scheme through a two-step selection process. Firstly, the purpose of the experiments was to test whether small-angle rotations would introduce animal motion. So a scan scheme with more rotation steps was preferred. This left us the G5 and R5 schemes. Secondly, the homemade octagon collimator-tube assembly was asymmetric and, when placed in the detector gantry, it was off-centered from the axial axis. Therefore, practically it was easier to design a G5 scheme that would avoid possible collision between the animal bed and the walls of the octagon collimator tube.

For the experimental study, the energy window used was 120–160 keV for ^{99m}Tc. An OS-EM algorithm with eight subsets was used to reconstruct the experimental data. The iteration number was selected empirically. The system matrix used was derived from Monte Carlo simulation (Yao *et al* 2009). The voxel size of the reconstructed image was $0.25 \times 0.25 \times 1$ mm^3.

3. Results

3.1. Monte Carlo simulated phantom studies

Figure 7 shows the reconstructed images of the ultra-micro hot-rod phantom scanned with each scheme. Each image is labeled with the scan scheme code used to obtain the simulation data. The 0.75 mm hot-rod sections (at 3 o'clock position) from the R1 and G1 schemes are more blurred than that with other schemes. For example, the images from the R2–R5 scan schemes have better hot-rod identification in the outer column of the 0.75 mm section than R1 scheme does. Another observation is that, in any column with two images, e.g. the 1 o'clock section, the top image is slightly clearer than the bottom image. In other words, the R group of scan schemes outperforms the G group of scan scheme group, given the same number of rotation steps are used.

The reconstructed images of the grid-patterned hot-rod phantom study are shown in figure 8. To reduce statistical noise, the images shown are from a summation of 30 transaxial slices which corresponds to 30 mm in thickness.

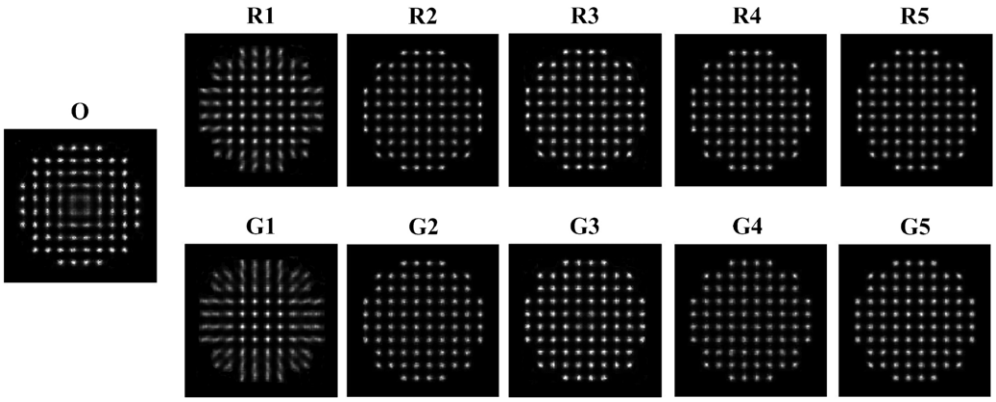

Figure 8. Reconstructed images of the simulated grid-patterned hot-rod phantom studies. The code names of the scan schemes used for acquiring each scan are indicated above the corresponding image.

In the image acquired with the O scan scheme, the four rods at the center of FOV are severely blurred, i.e. this region is significantly inferior to that at the edge of FOV in terms of resolution. For the images acquired with the R1 and G1 schemes, the cylinders in the central area are sharp while those near the borders are blurred. The middle two rows of rods show clearly that the horizontal resolutions improve from the edges to the center of FOV. The image of the R1 scheme shows better resolution in the edge areas than that of the G1 scheme. As compared to the images from the O, R1 and G1 schemes, the images acquired with the other HRT schemes show overall superior image quality, and there is much less variation in terms of horizontal or vertical resolution.

The $IR(\beta)|_{\beta=0}$ images and the corresponding central horizontal section profiles are shown in figure 9. In both the images and profiles, the O, R1 and G1 schemes show clear variation over the horizontal FOV, while the other schemes look more or less uniform over the range.

3.2. Analytical indices and correlation with image resolution

Figures 10(a) and (b) show the performance comparison of the R and G scan schemes, respectively, using the hypothetical scan results of the 25 mm diameter disc. For each HRT scan scheme, the *SC*, *S*, *SR*, and $DR(\beta)|_{\beta=0}$ and $IR(\beta)|_{\beta=0}$ values in the FOV are displayed as images in incremental rows in one column. The results of the O scheme, the conventional scan scheme, are shown in the first column of both figures 10(a) and (b) to serve as a reference. The horizontal section profiles passing the center of the *SC*, *S*, *SR* and $DR(\beta)|_{\beta=0}$ images in figure 10 are extracted and compared in figure 11. The results in figures 10 and 11 are arranged in parallel—the profiles in figures 11(a) and (b) are from the images in figures 10(a) and (b), respectively.

It can be seen from the first rows of figures 10(a) and (b), and accordingly in figures 11(a) and (b), that except for R1 and G1, the rest of eight HRT schemes have similar *SC* values as compared to the O scheme. The sensitivity performances of all schemes are also very close, as shown in figures 10 and 11. For the scan schemes studied, the average sensitivity values over the FOV vary within a very small range, from 3.55×10^{-4} to 3.64×10^{-4}. The maximum sensitivity loss of the R and G schemes studied, as compared to the O scheme, is less than 3%.

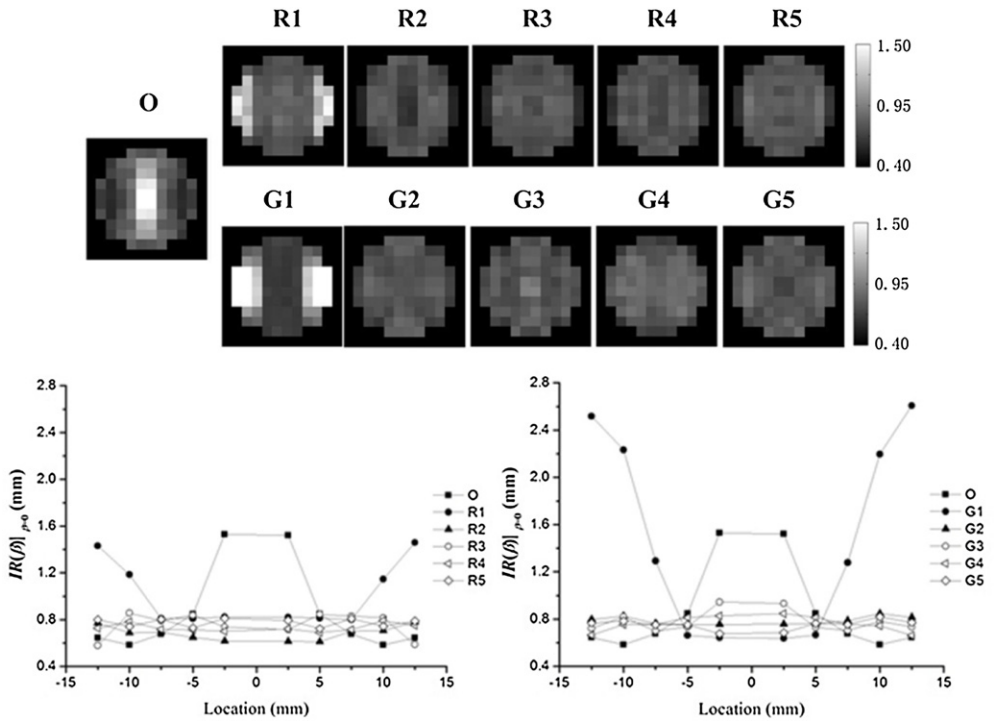

Figure 9. Top: the $IR(\beta)|_{\beta=0}$ images derived from the hot-rod phantom images in figure 8. Bottom: the central horizontal section profiles extracted from the $IR(\beta)|_{\beta=0}$ images on top.

The row of *SR* images in figure 10(a) shows that the O and R scan schemes have similar pattern and little visible differences. In figure 11(a), the *SR* profiles of R1 to R5 schemes overlap with each other and appear as a single curve, and the profile of the O scheme is slightly higher than that of the R schemes. So there is little difference among R schemes and they are all slightly better than the O scheme in terms of *SR*. By observing the row of *SR* images in figure 10(b) and accordingly in figure 11(b), similar conclusions can be drawn for the G1 to G5 schemes, i.e. there is a little difference among them and they are all slightly better than the O scheme.

All the $DR(\beta)|_{\beta=0}$ images in figure 10 show little variations in the horizontal direction or unique feature that is visually prominent. The corresponding section profiles in figure 11, however, reveal that variations and differences do exist. As compared to the section profiles of *SR* images, $DR(\beta)|_{\beta=0}$ shows larger difference between scan schemes. The O scheme has a bell shape that is different from all other schemes, and its values in the central peak area are higher than all other schemes. This means that all the HRT schemes have improved resolution in the central area as compared to the O scheme, as shown in figure 8. The other schemes share a shape of a bowl with an elevated central area; the relative heights of the central area and the borders of the bowl vary depending on the scan scheme. Among the R and G group HRT scan schemes, respectively, R1 and G1 have the highest and R2 and G2 have the lowest $DR(\beta)|_{\beta=0}$ profiles; the differences between other schemes are clearly smaller. According to their $DR(\beta)|_{\beta=0}$ profiles, R1 and G1 schemes show sharp resolution degradation trend toward the FOV edge. For R and G schemes with matching number of rotations per each translation

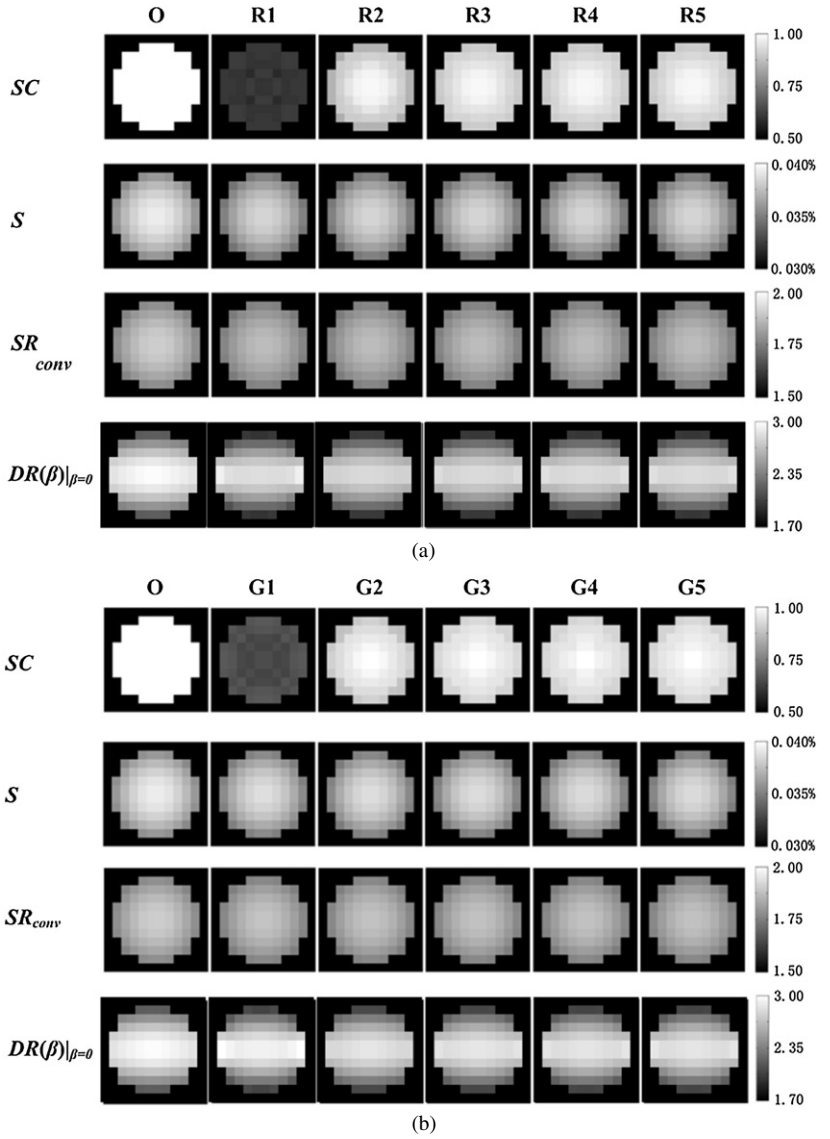

Figure 10. Pixelwise performance indices of the ten HRT and the O scan schemes displayed in two panels. In each panel, each column corresponds to one scan scheme, each row corresponds to a performance index. (a) R and O schemes. (b) G and O schemes.

step, an R scheme in figure 11(a) has lower $DR(\beta)|_{\beta=0}$ values than its G scheme counterpart in figure 11(b).

By comparing the representative curve patterns of the $IR(\beta)|_{\beta=0}$ and $DR(\beta)|_{\beta=0}$ profiles, i.e. those of O, R1 and G1, the *DR* and *IR* show clear resemblance while *SR* and *IR* do not. The joint-NMSE values between *IR* and *SR*, and *IR* and *DR*, are 0.0767 and 0.0665, respectively. This indicates quantitatively that the corresponding $DR(\beta)|_{\beta=0}$ images match $IR(\beta)|_{\beta=0}$ better than the *SR* images do. Since $IR(\beta)|_{\beta=0}$ results represent what is measured by the imaging system, in other words the gold standard of predictive indices, its closeness

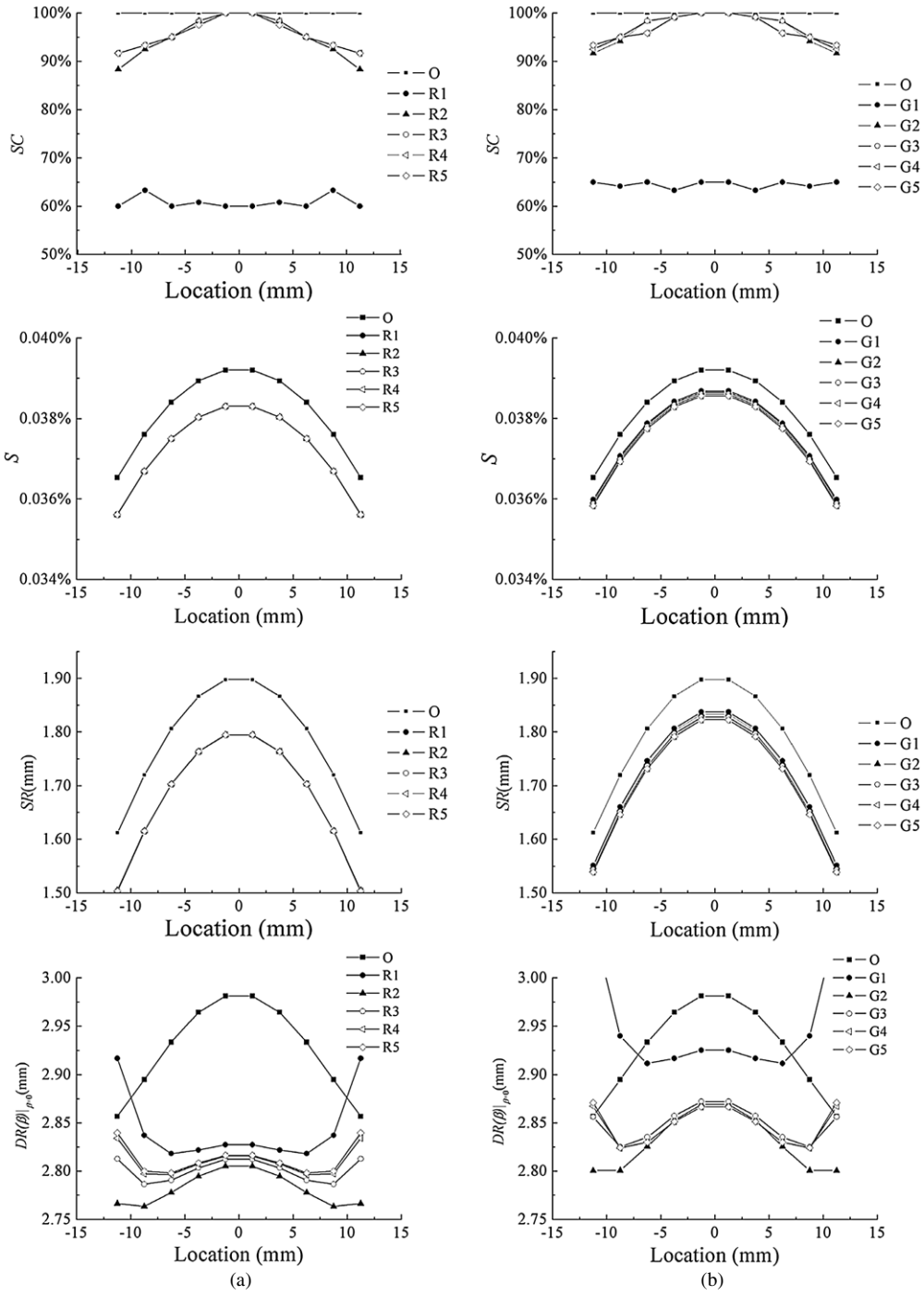

Figure 11. Central horizontal section profiles extracted from the *SC*, *S*, *SR*, $DR(\beta)|_{\beta=0}$ and $IR(\beta)|_{\beta=0}$ images in figure 11. (a) R and O schemes. (b) G and O schemes.

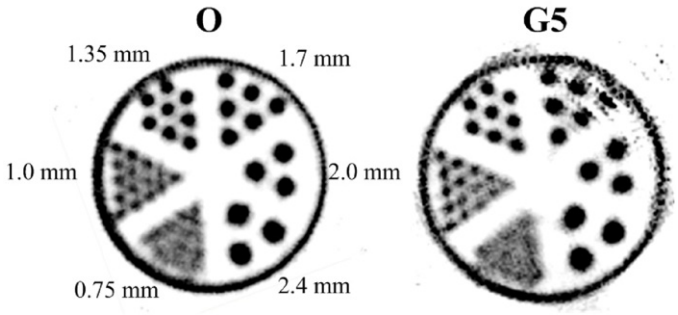

Figure 12. Experimental hod-rod phantom results acquired with (a) the convertional rotation O and (b) the HRT G5 scheme.

to $DR(\beta)|_{\beta=0}$ therefore indicate that $DR(\beta)$ is a more relevant resolution performance index than the traditional *SR* definition.

The row of $DR(\beta)|_{\beta=0}$ images shown in figure 10 do not show a circular symmetry. This is different from the images of *SC*, *S* and *SR* but is expected. For example, the $DR(\beta)|_{\beta=0}$ values for the rods on the central horizontal line are *radial* direction resolution, the $DR(\beta)|_{\beta=0}$ values for the rods on the central vertical line are *tangential* direction resolutions. They should not be the same. But the $DR(\beta)|_{\beta=0}$ values along the central horizontal line and the $DR(\beta)|_{\beta=\pi/2}$ values along the central vertical line are the same, because they are both radial direction resolutions.

3.3. Experimental phantom study

Figure 12 shows the images of the ultra-micro hot-rod phantom scanned with the O (left) and the G5 (right) schemes. The 1 mm diameter hot-rod is the smallest that is distinguishable in both images. No imaging resolution loss is observed with the HRT-G5 orbit compared to the O orbit. The zigzag artifacts along the top-right ring area of the phantom might be caused by inadequate projection sampling introduced when the phantom was placed off-center of FOV in the imperfect home-made octagon collimator tube.

4. Discussion

The goal of this work was to determine a scan scheme for an animal SPECT system with a stationary detector gantry. Intuitively, the rotational movement of animal should be completely avoided, or at least be minimized to facilitate *in vivo* animal scan. But on this SPECT system, the collimator cannot provide adequate projection views with a stationary-object scanning protocol. So a scan protocol that would provide tomographic data acquisition and minimize the animal rotation is required. The HRT scan schemes were proposed to satisfy these requirements. For these new scan schemes, it is important to evaluate their efficacy and find the better one. To facilitate the assessment, we have defined sampling completeness (*SC*), sensitivity (*S*), conventional system resolution (*SR*), directional resolution (DR (β)) as the figures-of-merit. We used the image resolution measures from a phantom study, IR (β), for assessing and comparing the validity of the DR (β) and *SR*.

4.1. What is new in DR

The conventional *SR* was originated from imaging systems with a parallel-hole collimator and the filtered back-projection reconstruction algorithm. It assumes that when a projection is back-projected into image space, the spread is only along the direction parallel to the original projection upon the detector. This is not true as clearly shown in figure 6 with the pinhole-based illustration—the spread is a function of orientation angle β. To address this issue, the directional resolution concept was devised for better quantifying the resolution performance in this study. Two factors contribute to the current form of $DR(\beta)$ in (13): (a) an orientation-related resolution model $DR_{i,j}(\beta)$ for each scan stop, which replaces the conventional orientation-isotropic resolution model $SR_{i,j}$; and (b) a new approach to combine $DR_{i,j}(\beta)$ into one $DR(\beta)$, the contribution from individual projection is inversely related to the projection' spread (or resolution $DR_{i,j}(\beta)$) and proportionally related to the projection's magnitude (sensitivity, $S_{i,j}$). As mentioned, the choice of using the reciprocal of $DR_{i,j}(\beta)$ is due to its possible infinite values in certain projection directions.

It is apparent that equations (13) and (6) calculate the average resolution indices differently. To exclude the effect of this difference in the comparison of *DR* and *SR*, we also calculated the average *SR* with an analogous form of average *DR*

$$SR = \left[\frac{\sum_{j=1}^{J} \sum_{i=1}^{I} S_{i,j}^{q} SR_{i,j}^{p}}{\sum_{j=1}^{J} \sum_{i=1}^{I} S_{i,j}^{q}} \right]^{\frac{1}{p}} \Bigg|_{p=-1,q=3}$$

The joint NMSE between this new *SR* and $IR(\beta)|_{\beta=0}$ was 0.0790, it is higher than the joint NMSE between $DR(\beta)|_{\beta=0}$ and $IR(\beta)|_{\beta=0}$. This confirms that *DR* is a more relevant measure of resolution than *SR*.

Although it is highly desired, the $DR(\beta)$ as presented in this work is not an absolute quantitative resolution index. To design a resolution index with features of $DR(\beta)$ and also the absolute resolution performance, is a direction for future research.

4.2. Axial consideration

For a slit-slat collimator-based SPECT system, its axial resolution may be considered to be independent of the transverse in-plane resolution (Metzler *et al* 2006). For this reason, axial movements and resolution evaluations were not included in this study. Compared to that in the transverse plane, the sampling design and performance evaluation in the axial direction are 1D tasks. A standard way to implement axial direction sampling is through using a helical scan scheme. In the case of the add-on SPECT in this study, this could be accomplished by adding object movements along the axial axis. The net effect of a helical scan in terms of axial sampling is that the scan would expose an image object to multiple detectors—or to the same detector but placed at multiple positions. The overall effect of this multiple detector or position sampling is that the axial variation of the detector responses, either for individual image voxels or the image object as a whole, is averaged out so that the system could achieve a more uniform axial imaging performance.

5. Conclusion

In this work, we assessed the performance of ten HRT scan schemes for *in vivo* animal imaging on a stationary detector SPECT system. Four analytic evaluation indices, *SC*, *S*, *SR* and $DR(\beta)$ were used to quantify the performance of each scan scheme in each point

of the FOV. The directional resolution index $DR(\beta)$ is a new index that we introduced to account for the effect of the relative orientation between the measured projection and its back-projected image distribution. For all the scan schemes, a grid-patterned hot-rod phantom was simulated to extract the spatial resolution performance, which served as a reference for comparing the predictive value of the conventional index *SR* and the new resolution index $DR(\beta)$. A selected HRT scan scheme was tested with an experimental phantom study.

Eight of ten HRT schemes evaluated showed close to 100% sampling completeness, and achieved better resolution than the conventional full-angle rotation-only scheme with negligible sensitivity loss. The $DR(\beta)$ values calculated show closer resemblance to the resolution measures from the simulated phantom. The experimental phantom image obtained was satisfactory. Since the rotation steps in the selected HRT schemes are limited to a small angle range, e.g. -10° to 10°, the gravity impact can be significantly reduced for *in vivo* animal imaging. We conclude that it is feasible to perform *in vivo* animal imaging with a HRT scan scheme, and *SC* and *DR* are useful predictors for quantitatively assessing the performance of a scan scheme.

Acknowledgments

This work was partially supported by the Specialized Research Fund for the Doctoral Program of Higher Education (SRFDP200800031071), the National Natural Science Foundation of China (no 10675069), and the Roswell Park Alliance Foundation under grant 62-2426-01.

Appendix

The p and q values in (13) were determined through the following numerical searching procedure.

First, a value from the list $\{-3, -2, -1.5, -1, -0.5, -0.25\}$ and a value from the list $\{-5, -3, -2, -1, -0.5, 0.5, 1, 2, 3, 5\}$ were selected and assigned to p and q, respectively. Since $DR(\beta)|_{\beta=0}$ may be infinite when $p > 0$, only the negative cases of p were calculated. Consequently, there were a total of 60 (p, q) pairs. The values of each (p, q) pair was used to calculate a $DR(\beta)|_{\beta=0}$ image for all the scan schemes described in table 1, as well as the conventional rotation-only scheme. The $DR(\beta)|_{\beta=0}$ images were then compared to the $IR(\beta)|_{\beta=0}$ resolution image by calculating the joint NMSE as defined in (15). The (p,q) pair that yielded the minimal joint NMSE was first identified.

Figure A.1 shows the plot of the joint-NMSE values between $IR(\beta)|_{\beta=0}$ and $DR(\beta)|_{\beta=0}$ with the 60 (p, q) pair values. It can be seen that for all the q values except $q = 2$ and $q = 5$, the minimal joint-NMSE values occur when p is -1. Therefore p was assigned the value -1.

The graph in figure A.2 shows the joint-NMSE values between $IR(\beta)|_{\beta=0}$ and $DR(\beta)|_{\beta=0}$ as p was fixed at -1 and q value changed from -10 to 10 with a fine sampling interval of 0.2. The q value that gives the minimal joint NMSE is 3. Therefore q was assigned the value of 3 in (13). The joint NMSE between $IR(\beta)|_{\beta=0}$ and *SR* as a function of q is also shown for comparison. Here *SR* was calculated from the analogous form of *DR*, as shown near the end of section 4.1. With the $p = -1$ and $q = 3$, it is clear that the $DR(\beta)|_{\beta=0}$ image is closer to $IR(\beta)|_{\beta=0}$ image than *SR*.

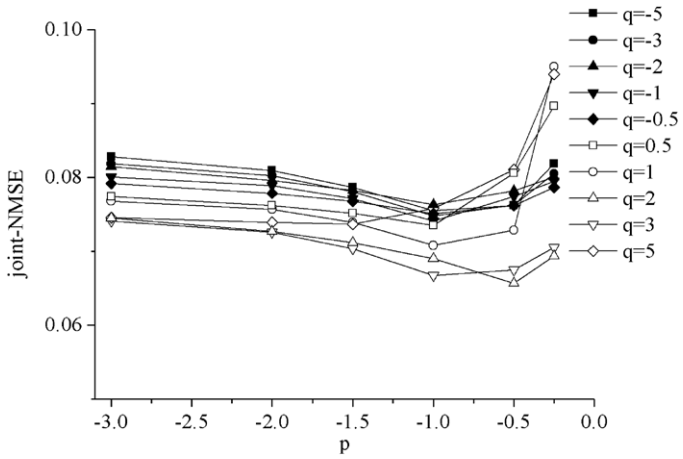

Figure A.1. To search the p and q values that yield the minimal joint NMSE. $p = -1$ was selected as it paired well with most q values shown according to this criterion.

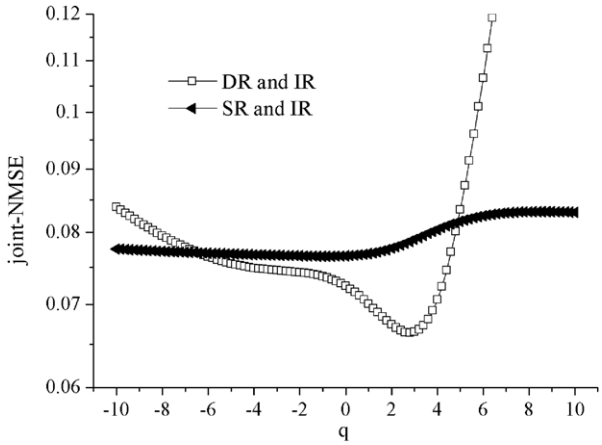

Figure A.2. The joint-NMSE values between the $DR(\beta)|_{\beta=0}$ and $IR(\beta)|_{\beta=0}$ images are plotted as functions of q when p was set to -1. The joint-NMSE values between the SR and $IR(\beta)|_{\beta=0}$ images are also plotted for comparison.

References

Accorsi R, Novak J R, Ayan A S and Metzler S D 2008 Derivation and validation of a sensitivity formula for slit-slat collimation *IEEE Trans. Med. Imaging* **27** 709–22

Beekman F J and Vastenhouw B 2004 Design and simulation of a high-resolution stationary SPECT system for small animals *Phys. Med. Biol.* **49** 4579–92

Beekman F J, van der Have F, Vastenhouw B, van der Linden A J A, van Rijk P P, Burbach J P H and Smidt M P 2004 U-SPECT-I: a stationary molecular imaging system for small animals with 0.1 micro-litre resolution *IEEE Nucl. Sci. Symp. Med. Imag. Conf. Rec.* vol 4 pp 2263–7

Chang W, Ordonez C E, Liang H, Li Y and Liu J 2009 C-SPECT—a clinical cardiac SPECT/Tct platform: design concepts and performance potential *IEEE Trans. Nucl. Sci.* **56** 2659–71

DiFilippo F P 2008 Design and performance of a multi-pinhole collimation device for small animal imaging with clinical SPECT and SPECT-CT scanners *Phys. Med. Biol.* **53** 4185–201

Jan S *et al* 2004 GATE: a simulation toolkit for PET and SPECT *Phys. Med. Biol.* **49** 4543–61

Laforest R, Longford D, Siegel S, Newport D F and Yap J 2007 Performance evaluation of the microPET-FOCUS-F120 *IEEE Trans. Nucl. Sci.* **54** 42–9

Li Y, Oldendick J, Ordonez C E and Chang W 2009 The geometric response function for convergent slit-slat collimators *Phys. Med. Biol.* **54** 1469–82

Ma T, Yao R, Shao Y and Zhou R 2009 A SVD-based method to assess the uniqueness and accuracy of SPECT geometrical calibration *IEEE Trans. Med. Imaging* **28** 1929–39

Mahmood S T, Erlandsson K, Cullum I and Hutton B F 2009 Design of a novel slit-slat collimator system for SPECT imaging of the human brain *Phys. Med. Biol.* **54** 3433–49

Meikle S R, Kench P, Kassiou M and Banati R B 2005 Small animal SPECT and its place in the matrix of molecular imaging technologies *Phys. Med. Biol.* **50** 45–61

Metzler S D, Accorsi R, Novak1 J R, Ayan A S and Jaszczak R J 2006 On-axis sensitivity and resolution of a slit-slat collimator *J. Nucl. Med.* **47** 1884–90

Metzler S D, Greer K L and Jaszczak R J 2003a Helical pinhole SPECT for small-animal imaging: a method for addressing sampling completeness *IEEE Trans. Nucl. Sci.* **50** 1575–83

Metzler S D, Bowsher J E and Jaszczak R J 2003b Geometrical similarities of the Orlov and Tuy sampling criteria and a numerical algorithm for assessing sampling completeness *IEEE Trans. Nucl. Sci.* **50** 1550–5

Metzler S D and Jaszczak R J 2006 Simultaneous multi-head calibration for pinhole SPECT *IEEE Trans. Nucl. Sci.* **53** 113–20

Novak J R, Ayan A S, Accorsi R and Metzler S D 2008 Verification of the sensitivity and resolution dependence on the incidence angle for slit-slat collimation *Phys. Med. Biol.* **53** 953–66

Orlov S S 1976 Theory of three-dimensional reconstruction: I. Conditions for a complete set of projections *Sov. Phys. Crystallogr.* **20** 312–4

Radon J 1986 On the determination of functions from their integral values along certain manifolds *IEEE Trans. Med. Imaging* **5** 170–6

Rogers W L *et al* 1982 SPRINT: a stationary detector single photon ring tomograph for brain imaging *IEEE Trans. Med. Imaging* **1** 63–8

Shao Y, Yao R, Ma T and Manchiraju P 2007 Initial studies of PET-SPECT dual-tracer imaging *IEEE Nucl. Sci. Symp. Med. Imag. Conf. Rec.* vol 6 pp 4198–204

Vastenhouw B and Beekman F 2007 Submillimeter total-body murine imaging with U-SPECT-I *J. Nucl. Med.* **48** 487–93

Walrand S, Jamar F, de Jong M and Pauwels S 2005 Evaluation of novel whole-body high-resolution rodent SPECT (Linoview) based on direct acquisition of linogram projections *J. Nucl. Med.* **46** 1872–80

Yao R, Ma T and Shao Y 2009 Derivation of system matrix from simulation data for an animal SPECT with slit-slat collimator *IEEE Trans. Nucl. Sci.* **56** 2651–58